Int J Adv Manuf Technol (2016) 86:1037–1054
DOI 10.1007/s00170-015-8129-4

ORIGINAL ARTICLE

An effective time domain model for milling stability prediction simultaneously considering multiple modes and cross-frequency response function effect

Xiaowei Tang[1] · Fangyu Peng[2] · Rong Yan[1] · Yanhong Gong[1] · Xin Li[1]

Received: 15 July 2015 / Accepted: 12 November 2015 / Published online: 4 January 2016
© Springer-Verlag London 2015

Abstract The dynamic properties of the machine tool structure usually contain multiple modes and significant cross-frequency response functions whose vibration in one direction is caused by a force in the orthogonal direction. To simplify the stability prediction model, the stability of a milling process has been traditionally predicted in the time domain by selecting only the most flexible mode and neglecting the cross-frequency response functions. This paper proposes an effective stability prediction model simultaneously considering multiple modes and the cross-frequency response functions in the time domain. When introducing the cross-frequency response functions, mechanical mobility and impedance transformation method dealing with measured frequency response functions is proposed to establish the dynamic matrix equation. In considering the multiple modes, the approaches of multiple modal parameter normalization on the tool tip and reducing the vibration variable number in modal space are described in detail. The comparisons of numerical simulation results between the proposed method and the frequency domain method demonstrate the effectiveness of the proposed model. A cutting experiment produces results in agreement with the theoretical prediction. The analysis of the numerical simulation and the experimental data indicates that the multiple modes have great effect on stability boundary. Additionally, it also shows that the cross-frequency response functions influence the stability boundary increasingly along with the increasing amplitude ratio of the cross-frequency response functions and direct frequency response functions.

Keywords Stability prediction · Time domain · Multiple modes · Cross-frequency response functions

✉ Rong Yan
yanrong@hust.edu.cn

[1] National Numerical Control System Engineering Research Centers, Huazhong University of Science and Technology, Wuhan 430074, China

[2] State Key Lab of Digital Manufacturing Equipment and Technology, Huazhong University of Science and Technology, Wuhan 430074, China

1 Introduction

As one of the most common phenomena during many machining operations, chatter has significantly negative effect on productivity and quality guarantee of parts [1, 2]. Accurate prediction of the stability lobe diagram is very important to avoid the machining chatter and thus improve the productivity and part surface quality [3, 4]. The milling stability is related to the dynamic properties of the machine tool structure. The frequency response functions (FRFs) representing the dynamic properties at the tool end point usually contain multiple modes and have significant cross-FRFs whose vibration in one direction is caused by a force in the orthogonal direction. The two factors both effect the accurate prediction of the milling stability.

Solis and Peres et al. [5] combined chatter's analytical prediction method with experimental multi-degree-of-freedom (MDOF) system modal analysis. Mann et al. [6] simultaneously investigated the milling stability and surface location error of a multiple mode system by employing the temporal finite element analysis method. Tang et al. [7] proposed an analytical stability prediction method with MDOF system modal analysis and demonstrated the multi-mode interaction on stability prediction. Wan et al. [8] developed a dynamic model for milling processes dominated by

multiple modes and analyzed the effect of the multiple modes on stability boundary. Berglind and Ziegert [9] developed an analytical time domain model to predict the motion of a multi-mode cutting tool during orthogonal turning operations. Cao et al. [10] found that the gyroscopic moment of the spindle shaft can increase the cross-FRFs which influence the stability boundary obtained by Nyquist stability criterion. Zhang [11] investigated the cross-FRF coupling and revealed that the cross-FRF coupling has a great effect on stability prediction during the practical milling process. As a precondition for the accurate prediction of the chatter, the multi-mode interaction and cross-FRF effect should both be considered in the stability prediction model when the cross-FRFs have significant magnitude compared with the direct cross-FRFs.

Using frequency domain methods, such as the zero-order approximation (ZOA) method [12] and the multi-frequency (MF) method [13, 14], stability prediction considering multi-mode interaction can be achieved by scanning the chatter frequencies around all of the dominant modes of the FRFs. The eigenvalue equation of the frequency domain methods can contain the cross-FRFs. In addition to the frequency domain methods, there are also many time domain methods for the stability prediction, such as the temporal finite element analysis (TFEA) method [15], the semi-discretization method (SDM) [16, 17], the full-discretization method (FDM) [18], the numerical integration method [19, 20], and the Runge-Kutta methods [21]. Although frequency domain solution can efficiently predict stability lobe simultaneously considering multiple modes and cross-FRF effect, the time domain methods have advantages of being applicable to various machining conditions, such as cutter run-out, surface location error, and stable isolated zones. Gradišek et al. [22] investigated the additional type of instability causing periodic chatter that is predicted only by the time domain method SDM. Mann et al. [23] proved the unstable islands in the stability charts and predicted the surface location error by an updated TFEA. Munoa et al. [24] studied the stability of a two-mode milling process, indicating that the MF method and the SDM lead to the same exact solution in all cases while the MF method has problems in determining stable isolated zones.

When the multiple modes and cross-FRFs are considered simultaneously, the time domain modal will be complex and difficult to solve. In previous stability studies in the time domain, to simplify the prediction model, the stability of a milling process dominated by multiple modes was traditionally predicted by selecting only the most flexible mode and neglecting the cross-FRFs, alternatively, separating the multiple modes and the cross-FRFs. To obtain a more accurate stability lobe in the time domain, this paper proposes an effective stability model in the time domain simultaneously considering multi-mode interaction and the cross-FRF effect. Due to the introduction of the cross-FRFs, the mechanical mobility and impedance transformation method dealing with measured FRF is proposed to establish the dynamic matrix equation. Due to the consideration of the multiple modes, the approaches of multiple modal parameter normalization on the tool tip and reducing vibration variable number in modal space are described. The stability lobe diagrams obtained by the proposed time domain model and the ZOA method are compared to verify the availability of the proposed model, and cutting experiments are performed to verify the accuracy of the stability prediction. The structure of the paper is as follows. In Sect. 2, the derivation of the stability model formulations of multi-mode system considering the cross-FRFs is provided in detail. In Sect. 3, the numerical simulation and comparison of the proposed model and the ZOA method are provided. Additionally, the effect of the multiple modes and cross-FRFs on the stability boundary is analyzed. The modal parameter identification and experimental verification are provided in Sect. 4. Finally, the conclusions are presented in the last section.

2 Stability model of the multi-mode system

2.1 Mechanical mobility and impedance transformation approach for dynamic equation

A schematic milling system dominated by multiple modes is shown in Fig. 1. To simplify the milling process dynamics and focus on the modeling of the multi-modes and cross-FRF effect, the tool is assumed to be flexible compared with the rigid workpiece.

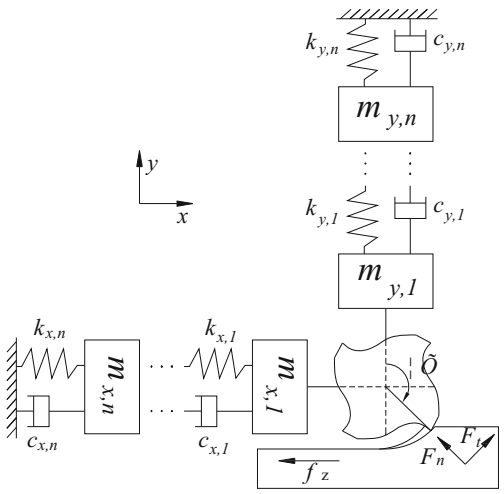

Fig. 1 Mechanical model (down-milling)

The modal impact test and the measured FRFs are illustrated in Fig. 2. It can be seen that the FRFs of the machine tool structure contain the direct FRFs H_{xx} and H_{yy} and the cross-FRFs H_{xy} and H_{yx}, and all of the FRFs have multiple modes.

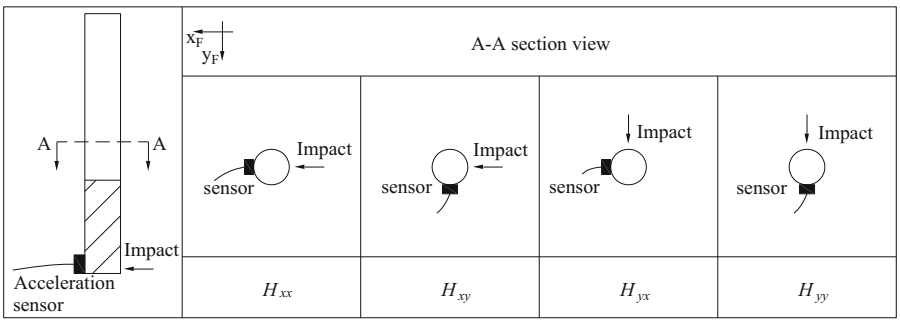

For the mechanical model in Fig. 1 and the measured FRFs in Fig. 2, the dynamic equation can be written in the frequency domain in the form of mechanical mobility (dynamic flexibility)

$$\begin{aligned} X(\omega) &= H_{xx}F_x(\omega) + H_{xy}F_y(\omega) \\ Y(\omega) &= H_{yx}F_x(\omega) + H_{yy}F_y(\omega) \end{aligned} \tag{1}$$

where $X(\omega)$ and $Y(\omega)$ denote the vibration of the tool tip in the x direction and y direction, respectively, and $H_{ij}(i,j=x,y)$ is the FRFs shown in Fig. 2. And, the subscript "ij" denotes the vibration in the i direction caused by the force in the j direction. $F_x(\omega)$ and $F_y(\omega)$ are the cutting forces.

In Eq. (1), the vibrations of the tool tip in the x direction and y direction contain two vibration components, respectively: one is contributed by the direct FRFs, and the other is contributed by the cross-FRFs, which cannot be integrated as a multi-dimension matrix equation only containing the total vibration variable of the tool tip. Therefore, Eq. (1) should be converted to the form of the mechanical impedance (dynamic stiffness).

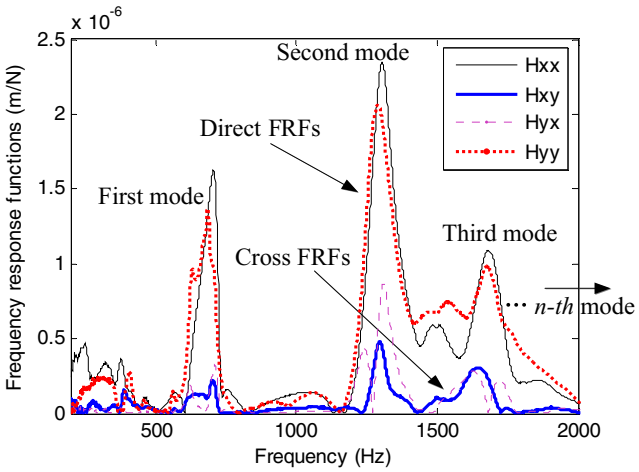

Fig. 2 Modal impact testing and frequency response functions

$$\begin{bmatrix} F_x(\omega) \\ F_y(\omega) \end{bmatrix} = \begin{bmatrix} H_{xx} & H_{xy} \\ H_{yx} & H_{yy} \end{bmatrix}^{-1} \begin{bmatrix} X(\omega) \\ Y(\omega) \end{bmatrix} = \begin{bmatrix} R_{xx} & R_{xy} \\ R_{yx} & R_{yy} \end{bmatrix} \begin{bmatrix} X(\omega) \\ Y(\omega) \end{bmatrix}$$
$$\Rightarrow \begin{cases} F_x(\omega) = R_{xx}X(\omega) + R_{xy}Y(\omega) \\ F_y(\omega) = R_{yx}X(\omega) + R_{yy}Y(\omega) \end{cases} \tag{2}$$

where the subscript ij of $R_{ij}(i,j=x,y)$ denotes the force in the i direction caused by the vibration in the j direction.

In contrast to Eq. (1), Eq. (2) contains two force components, respectively: one is contributed by the direct mechanical impedance, and the other is contributed by the cross-mechanical impedance. The force $F_i(\omega)(i=x,y)$ in Eq. (2) can be expressed as the sum of two forces

$$\begin{aligned} F_x(\omega) &= F_{xx}(\omega) + F_{xy}(\omega) \\ F_y(\omega) &= F_{yx}(\omega) + F_{yy}(\omega) \end{aligned} \tag{3}$$

where the subscript ij of $F_{ij}(\omega)(i,j=x,y)$ denotes the force in the i direction caused by the vibration in the j direction and

$$\begin{aligned} F_{xx}(\omega) &= R_{xx}X(\omega) \\ F_{xy}(\omega) &= R_{xy}Y(\omega) \\ F_{yx}(\omega) &= R_{yx}X(\omega) \\ F_{yy}(\omega) &= R_{yy}Y(\omega) \end{aligned} \tag{4}$$

According to the physical significance of the FRFs, Eq. (4) should be rewritten as the form of mechanical mobility (dynamic flexibility) again

$$\begin{aligned} X(\omega) &= \frac{1}{R_{xx}}F_{xx}(\omega) = H'_{xx}F_{xx}(\omega) \\ Y(\omega) &= \frac{1}{R_{xy}}F_{xy}(\omega) = H'_{yx}F_{xy}(\omega) \\ X(\omega) &= \frac{1}{R_{yx}}F_{yx}(\omega) = H'_{xy}F_{yx}(\omega) \\ Y(\omega) &= \frac{1}{R_{yy}}F_{yy}(\omega) = H'_{yy}F_{yy}(\omega) \end{aligned} \tag{5}$$

where the subscript ij of $H'_{ij}(i,j=x,y)$ denotes the vibration in the i direction caused by the force in the j direction.

Equation (5) can be converted to four multi-DOF dynamic systems in the time domain form as

$$\begin{cases} \boldsymbol{M}_{xx}\ddot{\boldsymbol{X}}(t)+\boldsymbol{C}_{xx}\dot{\boldsymbol{X}}(t)+\boldsymbol{K}_{xx}\boldsymbol{X}(t)=\boldsymbol{F}_{xx}(t) \\ \boldsymbol{M}_{xy}\ddot{\boldsymbol{Y}}'(t)+\boldsymbol{C}_{xy}\dot{\boldsymbol{Y}}'(t)+\boldsymbol{K}_{xy}\boldsymbol{Y}'(t)=\boldsymbol{F}_{xy}(t) \\ \boldsymbol{M}_{yx}\ddot{\boldsymbol{X}}'(t)+\boldsymbol{C}_{yx}\dot{\boldsymbol{X}}'(t)+\boldsymbol{K}_{yx}\boldsymbol{X}'(t)=\boldsymbol{F}_{yx}(t) \\ \boldsymbol{M}_{yy}\ddot{\boldsymbol{Y}}(t)+\boldsymbol{C}_{yy}\dot{\boldsymbol{Y}}(t)+\boldsymbol{K}_{yy}\boldsymbol{Y}(t)=\boldsymbol{F}_{yy}(t) \end{cases} \tag{6}$$

And

$$\begin{aligned} \boldsymbol{F}_{xx}(t)+\boldsymbol{F}_{xy}(t)&=\boldsymbol{F}_{x}(t) \\ \boldsymbol{F}_{yx}(t)+\boldsymbol{F}_{yy}(t)&=\boldsymbol{F}_{y}(t) \end{aligned} \tag{7}$$

where $\boldsymbol{M}_{ij}$, $\boldsymbol{C}_{ij}$, and $\boldsymbol{K}_{ij}(i,j=x,y)$ are the structure mass matrix, structure damping matrix, and structure stiffness matrix, respectively. The subscript ij denotes the force in the i direction caused by the vibration in the j direction.

$$\boldsymbol{M}_{ij}=\mathrm{diag}(\,m_{ij,1}\quad m_{ij,2}\quad m_{ij,3}\quad\cdots\quad m_{ij,n}\,)$$

$$\boldsymbol{C}_{ij}=\begin{bmatrix} c_{ij,1} & -c_{ij,1} & 0 & 0 & 0 \\ -c_{ij,1} & c_{ij,1}+c_{ij,2} & -c_{ij,2} & 0 & 0 \\ 0 & -c_{ij,2} & c_{ij,2}+c_{ij,3} & \ddots & 0 \\ 0 & 0 & \ddots & \ddots & -c_{ij,n-1} \\ 0 & 0 & 0 & -c_{ij,n-1} & c_{ij,n-1}+c_{ij,n} \end{bmatrix}$$

$$\boldsymbol{K}_{ij}=\begin{bmatrix} k_{ij,1} & -k_{ij,1} & 0 & 0 & 0 \\ -k_{ij,1} & k_{ij,1}+k_{ij,2} & -k_{ij,2} & 0 & 0 \\ 0 & -k_{ij,2} & k_{ij,2}+k_{ij,3} & \ddots & 0 \\ 0 & 0 & \ddots & \ddots & -k_{ij,n-1} \\ 0 & 0 & 0 & -k_{ij,n-1} & k_{ij,n-1}+k_{ij,n} \end{bmatrix} \tag{8}$$

where diag(*) stands for diagonal matrix.

The reason why Eq. (6) has four time domain vibration variables $\boldsymbol{X}(t)$, $\boldsymbol{Y}(t)$, $\boldsymbol{X}'(t)$, and $\boldsymbol{Y}'(t)$ can be explained as follows. The vibration variables $X(\omega)$ and $Y(\omega)$ in Eq. (5) denote the vibration of the tool tip, while the time domain vibration variables $\boldsymbol{X}(t)$, $\boldsymbol{Y}(t)$, $\boldsymbol{X}'(t)$, and $\boldsymbol{Y}'(t)$ in Eq. (6) denote the vibrations of the corresponding structure mass blocks with different modes. Note that only the first mass block denotes the tool tip. Then, it follows

$$\begin{aligned} \boldsymbol{X}(t)&=[\,x_1(t)\quad x_2(t)\quad x_3(t)\quad\cdots\quad x_n(t)\,]^{\mathrm{T}}, \\ \boldsymbol{X}'(t)&=[\,x_1(t)\quad x_2'(t)\quad x_3'(t)\quad\cdots\quad x_n'(t)\,]^{\mathrm{T}} \\ \boldsymbol{Y}(t)&=[\,y_1(t)\quad y_2(t)\quad y_3(t)\quad\cdots\quad y_n(t)\,]^{\mathrm{T}}, \\ \boldsymbol{Y}'(t)&=[\,y_1(t)\quad y_2'(t)\quad y_3'(t)\quad\cdots\quad y_n'(t)\,]^{\mathrm{T}} \end{aligned} \tag{9}$$

where $x_1(t)$ and $y_1(t)$ denote the vibrations of the tool tip and are equal to the vibration variables $X(\omega)$ and $Y(\omega)$ in Eq. (5).

The forces $F_x(\omega)$ and $F_y(\omega)$ in Eq. (5) denote the cutting forces on the tool tip, but the time domain vibration variables $\boldsymbol{F}_{xx}(t)$, $\boldsymbol{F}_{xy}(t)$, $\boldsymbol{F}_{yx}(t)$, and $F_{yy}(t)$ denote the forces on the corresponding structure mass blocks with different modes, and only the first mass block makes contribution to the cutting force on the tool tip. Thus

$$\boldsymbol{F}_{ij}(t)=\begin{bmatrix} f_{ij,1}(t) & 0 & 0 & \cdots & 0 \end{bmatrix}^{\mathrm{T}} \quad (i,j=x,y) \tag{10}$$

where $f_{xx,1}(t)+f_{xy,1}(t)=f_x(t)$ and $f_{yx,1}(t)+f_{yy,1}(t)=f_y(t)$ are equal to the cutting force on the tool tip in the x direction and y direction, respectively.

The cutting forces $f_x(t)$ in the x direction and $f_y(t)$ in the y direction are described as follows.

As seen in Fig. 3, every tooth of the tool is discretized in microelements along the axial cutting depth direction. Considering the helix angle β, the contact angle of each differential element varies with the change of the cutting depth. The instantaneous cutting angle of the pth differential element of the qth tooth is

$$\varphi_{pq}=\frac{2\pi\Omega}{60}t-\frac{z_p\tan\beta}{r}+q\frac{2\pi}{N} \tag{11}$$

where z_p is the coordinate of the pth element in the z direction, Ω denotes the spindle speed (rpm), r is the radius of the tool, and N is the number of teeth.

According to the mechanical force model [25], the cutting forces of a differential element in the tangential and normal directions are proportional to the chip load defined by the chip thickness $h(\varphi_{pq})$ and the axial depth dz.

$$\begin{aligned} dF_{t,pq}&=K_t h\left(\varphi_{pq}\right)g\left(\varphi_{pq}\right)dz \\ dF_{n,pq}&=K_n h\left(\varphi_{pq}\right)g\left(\varphi_{pq}\right)dz \end{aligned} \tag{12}$$

where $g(\varphi_{pq})$ is a unit step function determining whether the pth differential element of the qth tooth is cutting. K_t and K_n denote the cutting force coefficients in the tangential and radial directions, respectively.

The chip thickness $h(\varphi_{pq})$ consists of a static component due to the feed motion with the feed per tooth and a dynamic

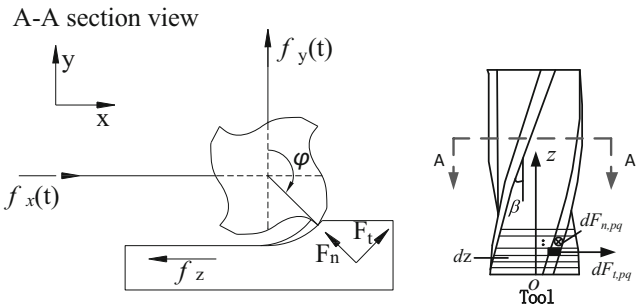

Fig. 3 Mechanical model

Table 1 Modal parameters for illustration

		Frequency (Hz)	Damping (%)	Residue
xx	First mode	701	5.63	9.129e−012−3.185e−004j
	Second mode	1293	3.13	−5.010e−011−1.586e−004j
xy	First mode	705	3.52	1.389e−010−1.186e−004j
	Second mode	1288	2.37	1.023e−012−0.682e−004j
yx	First mode	702	4.38	2.298e−012−1.504e−004j
	Second mode	1291	2.52	1.473e−011−0.755e−004j
yy	First mode	698	4.66	−7.544e−011−2.758e−004j
	Second mode	1295	2.88	−2.205e−010−1.560e−004j

component caused by the vibrations of the previous and current tool tooth. The static component does not affect the dynamic cutting thickness that generates chatter, so the chip thickness $h(\varphi_{pq})$ can be expressed by only the dynamic component as follows:

$$h\left(\varphi_{pq}\right) = \Delta x \sin\varphi_{pq} + \Delta y \cos\varphi_{pq} \tag{13}$$

where $T=60/(N\Omega)$ is the tooth passing period, $\Delta x=x_1(t)-x_1(t-T)$, $\Delta y=y_1(t)-y_1(t-T)$

The cutting forces of a differential element in the tangential and normal directions are translated into the x and y directions as

$$\begin{aligned} dF_{x,pq} &= dF_{t,pq}\cos\varphi_{pq} + dF_{n,pq}\sin\varphi_{pq} \\ dF_{y,pq} &= -dF_{t,pq}\sin\varphi_{pq} + dF_{n,pq}\cos\varphi_{pq} \end{aligned} \tag{14}$$

The resultant forces acting on the cutter are the integration of all of the infinitesimal cutting forces along the axial cutting depth direction.

$$\begin{aligned} f_x(t) &= \sum_{q=1}^{N} dF_{x,pq} \\ &= \sum_{q=1}^{N} \int_0^{a_p} \left(K_t\left(\Delta x\sin\varphi_{pq} + \Delta y\cos\varphi_{pq}\right)g\left(\varphi_{pq}\right)\cos\varphi_{pq} + K_n\left(\Delta x\sin\varphi_{pq} + \Delta y\cos\varphi_{pq}\right)g\left(\varphi_{pq}\right)\sin\varphi_{pq}\right)dz \\ f_y(t) &= \sum_{q=1}^{N} dF_{y,pq} \\ &= \sum_{q=1}^{N} \int_0^{a_p} \left(-K_t\left(\Delta x\sin\varphi_{pq} + \Delta y\cos\varphi_{pq}\right)g\left(\varphi_{pq}\right)\sin\varphi_{pq} + K_n\left(\Delta x\sin\varphi_{pq} + \Delta y\cos\varphi_{pq}\right)g\left(\varphi_{pq}\right)\cos\varphi_{pq}\right)dz \end{aligned} \tag{15}$$

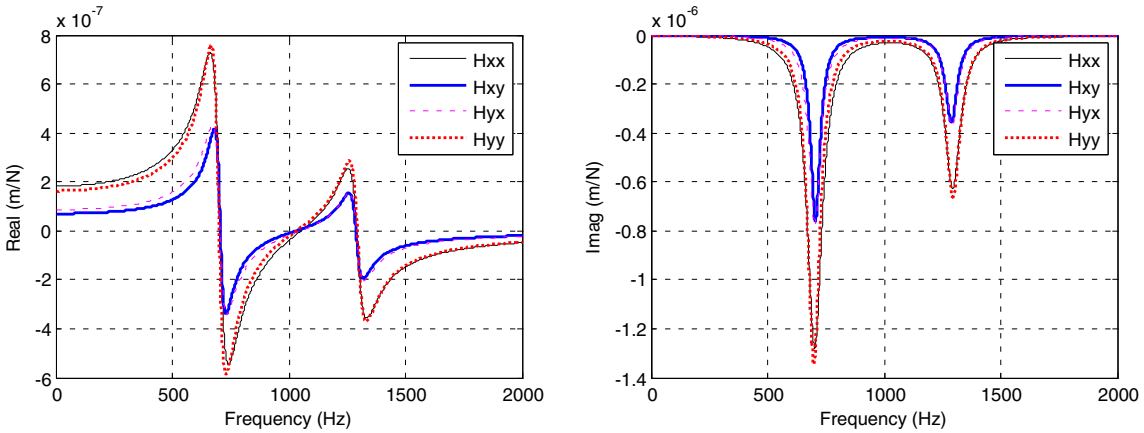

Fig. 4 Modal shapes fitted FRFs

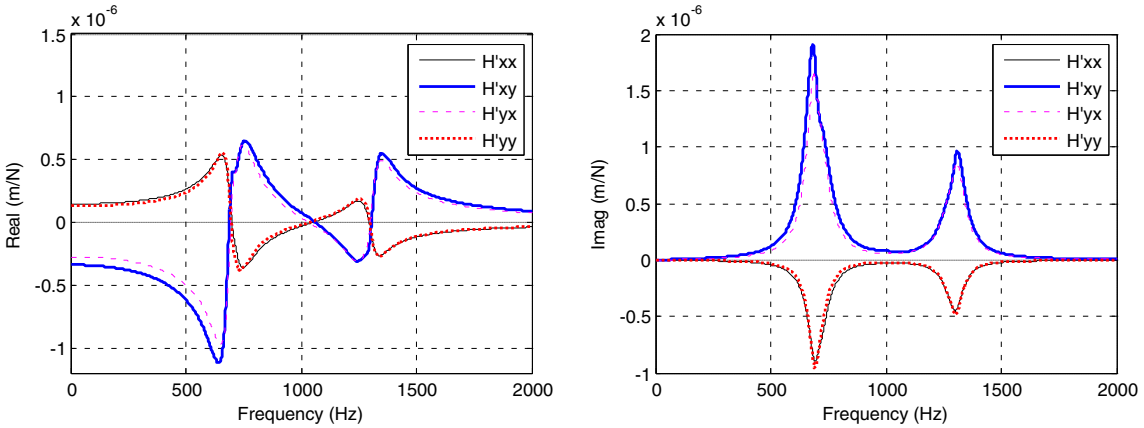

Fig. 5 FRFs H' calculated by the FRFs in Fig. 4

The cutting force on tool tip can be written as

$$\begin{bmatrix} f_x(t) \\ f_y(t) \end{bmatrix} = \begin{bmatrix} a_{xx} & a_{xy} \\ a_{yx} & a_{yy} \end{bmatrix} \begin{bmatrix} \Delta x \\ \Delta y \end{bmatrix} \tag{16}$$

$$\begin{aligned} a_{xx} &= \sum_{q=1}^{N} \int_0^{a_p} \left(K_t \sin\varphi_{pq} \cos\varphi_{pq} + K_n \sin^2\varphi_{pq} \right) g\left(\varphi_{pq}\right) dz \\ a_{xy} &= \sum_{q=1}^{N} \int_0^{a_p} \left(K_t \cos^2\varphi_{pq} + K_n \sin\varphi_{pq} \cos\varphi_{pq} \right) g\left(\varphi_{pq}\right) dz \\ a_{yx} &= \sum_{q=1}^{N} \int_0^{a_p} -\left(K_t \sin\varphi_{pq} \cos\varphi_{pq} - K_n \sin^2\varphi_{pq} \right) g\left(\varphi_{pq}\right) dz \\ a_{yy} &= \sum_{q=1}^{N} \int_0^{a_p} -\left(K_t \cos^2\varphi_{pq} - K_n \sin\varphi_{pq} \cos\varphi_{pq} \right) g\left(\varphi_{pq}\right) dz \end{aligned} \tag{17}$$

where a_p is the axial cutting depth.

At this point, the dynamic equation for the milling stability prediction simultaneously considering multiple modes and the cross-FRF effect has been established. However, according to Eq. (9), Eq. (6) has $4n$-2 vibration variables which should be reduced to $2n$. Thus, the modal space transformation is utilized to integrate the vibration variables in Eq. (6).

2.2 Modal space transformation

The vibration variables in Eq. (6) can be expressed in the modal coordinate as follows:

$$\begin{bmatrix} x_1 \\ x_2 \\ \vdots \\ x_n \end{bmatrix} = \begin{bmatrix} u_{xx,11} & u_{xx,12} & \cdots & u_{xx,1n} \\ u_{xx,21} & u_{xx,22} & \cdots & u_{xx,2n} \\ \vdots & \vdots & \cdots & \vdots \\ u_{xx,n1} & u_{xx,n2} & \cdots & u_{xx,nn} \end{bmatrix} \begin{bmatrix} q_{xx,1} \\ q_{xx,2} \\ \vdots \\ q_{xx,n} \end{bmatrix}, \begin{bmatrix} y_1 \\ y_2 \\ \vdots \\ y_n \end{bmatrix} = \begin{bmatrix} u_{xy,11} & u_{xy,12} & \cdots & u_{xy,1n} \\ u_{xy,21} & u_{xy,22} & \cdots & u_{xy,2n} \\ \vdots & \vdots & \cdots & \vdots \\ u_{xy,n1} & u_{xy,n2} & \cdots & u_{xy,nn} \end{bmatrix} \begin{bmatrix} q_{xy,1} \\ q_{xy,2} \\ \vdots \\ q_{xy,n} \end{bmatrix}$$

$$\begin{bmatrix} x_1 \\ x_2 \\ \vdots \\ x_n \end{bmatrix} = \begin{bmatrix} u_{yx,11} & u_{yx,12} & \cdots & u_{yx,1n} \\ u_{yx,21} & u_{yx,22} & \cdots & u_{yx,2n} \\ \vdots & \vdots & \cdots & \vdots \\ u_{yx,n1} & u_{yx,n2} & \cdots & u_{yx,nn} \end{bmatrix} \begin{bmatrix} q_{yx,1} \\ q_{yx,2} \\ \vdots \\ q_{yx,n} \end{bmatrix}, \begin{bmatrix} y_1 \\ y_2 \\ \vdots \\ y_n \end{bmatrix} = \begin{bmatrix} u_{yy,11} & u_{yy,12} & \cdots & u_{yy,1n} \\ u_{yy,21} & u_{yy,22} & \cdots & u_{yy,2n} \\ \vdots & \vdots & \cdots & \vdots \\ u_{yy,n1} & u_{yy,n2} & \cdots & u_{yy,nn} \end{bmatrix} \begin{bmatrix} q_{yy,1} \\ q_{yy,2} \\ \vdots \\ q_{yy,n} \end{bmatrix} \tag{18}$$

Table 2 Modal parameters identified by the FRFs in Fig. 5

		Frequency (Hz)	Damping (%)	Residue
xx	First mode	698	6.49	4.357e−006−2.545e−004 j
	Second mode	1298	3.46	−1.356e−006−1.250e−004 j
xy	First mode	683	7.58	−5.320e−005+5.836e−004j
	Second mode	1300	3.09	−2.452e−005+2.427e−004j
yx	First mode	690	6.43	−2.862e−005+4.545e−004j
	Second mode	1299	2.88	−9.478e−006+2.181e−004j
yy	First mode	694	4.78	4.048e−006−2.065e−004j
	Second mode	1300	3.18	−3.125e−006−1.231e−004j

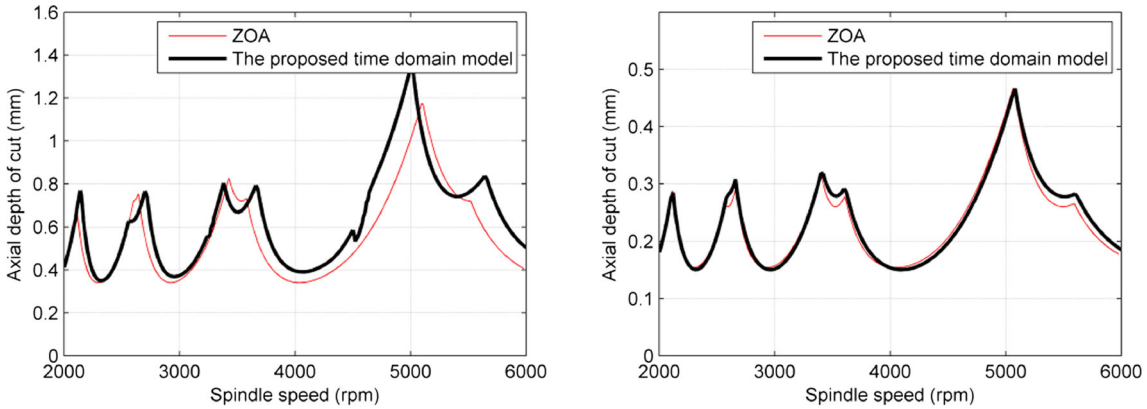

$a/D=0.5$ $a/D=1$

Fig. 6 Comparison of the stability lobes

where $u_{ij,lv}(i,j=x,y \quad l,v=1,2,\cdots,n)$ are the modal mass normalized shapes and $q_{ij,l}$ $(i,j=x,y \quad l=1,2,\cdots,n)$ are the modal coordinate.

Equation (18) provides the following constraints

$$\begin{aligned} x_1 &= u_{xx,11}q_{xx,1}+u_{xx,12}q_{xx,2}+\cdots+u_{xx,1n}q_{xx,n}=u_{yx,11}q_{yx,1}+u_{yx,12}q_{yx,2}+\cdots+u_{yx,1n}q_{yx,n} \\ y_1 &= u_{yy,11}q_{yy,1}+u_{yy,12}q_{yy,2}+\cdots+u_{yy,1n}q_{yy,n}=u_{xy,11}q_{xy,1}+u_{xy,12}q_{xy,2}+\cdots+u_{xy,1n}q_{xy,n} \end{aligned} \tag{19}$$

where x_1 and y_1 denote the vibrations of the tool tip and can indicate the occurrence of chatter. For the expression of x_1, $q_{xx,l}$ and $q_{yx,l}(l=1,2,\cdots,n)$ denote the components of the l-order natural frequency $\omega_{xx,l}$ and $\omega_{yx,l}(l=1,2,\cdots,n)$. For the linear structure, it is noted that $\omega_{xx,l}$ is equal to $\omega_{yx,l}(l=1,2,\cdots,n)$, which corresponds to the impact experiment results discussed later. Consequently, the following equations are deemed to be valid.

$$\begin{aligned} u_{xx,1l}q_{xx,l} &= u_{yx,1l}q_{yx,l} \\ u_{yy,1l}q_{yy,l} &= u_{xy,1l}q_{xy,l} \quad (l=1,2,\cdots,n) \end{aligned} \tag{20}$$

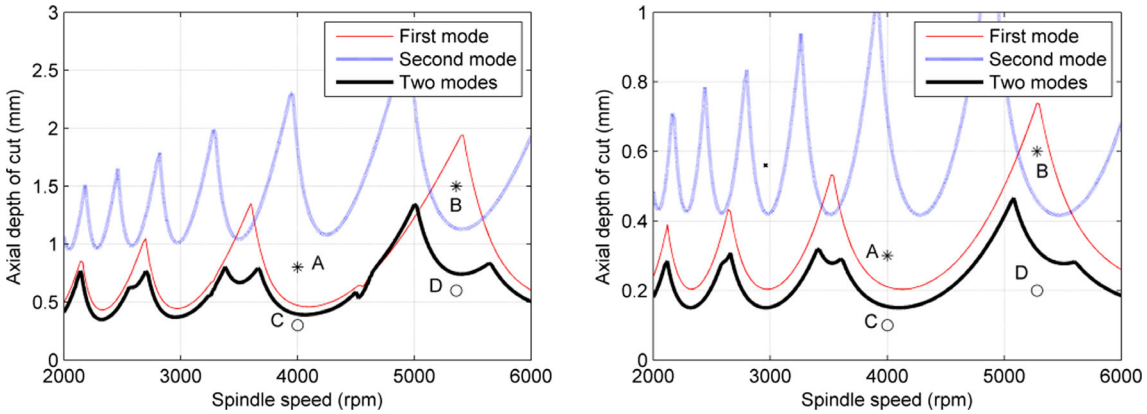

$a/D=0.5$ $a/D=1$

Fig. 7 The effect of multiple modes on the stability lobes. The *symbols* are as follows: (1) *open circle* is stable case and (2) *asterisk* is unstable case

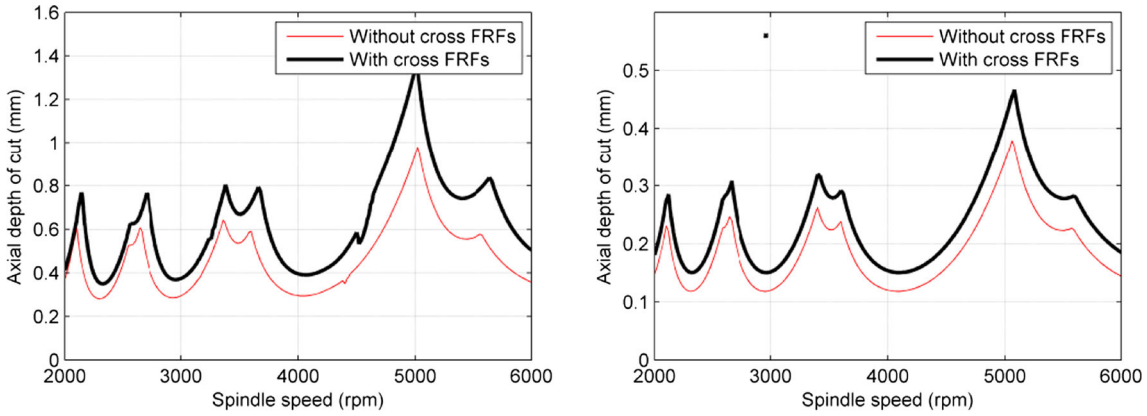

Fig. 8 Effect of cross-FRFs on the stability lobes

According to Eq. (20), $q_{yx,l}$ and $q_{xy,l}$ can be expressed by $q_{xx,l}$ and $q_{yy,l}(l=1,2,\cdots,n)$.

$$\begin{bmatrix} q_{yx,1} \\ q_{yx,2} \\ \vdots \\ q_{yx,n} \end{bmatrix} = \mathrm{diag}\left(u_{xx,11}/u_{yx,11} \quad u_{xx,12}/u_{yx,12} \quad \cdots \quad u_{xx,1n}/u_{yx,1n} \right) \begin{bmatrix} q_{xx,1} \\ q_{xx,2} \\ \vdots \\ q_{xx,n} \end{bmatrix}$$
$$\begin{bmatrix} q_{xy,1} \\ q_{xy,2} \\ \vdots \\ q_{xy,n} \end{bmatrix} = \mathrm{diag}\left(u_{yy,11}/u_{xy,11} \quad u_{yy,12}/u_{xy,12} \quad \cdots \quad u_{yy,1n}/u_{xy,1n} \right) \begin{bmatrix} q_{yy,1} \\ q_{yy,2} \\ \vdots \\ q_{yy,n} \end{bmatrix} \tag{21}$$

Next, Eq. (6) is transformed into the modal space by substituting Eq. (18) into Eq. (6) and utilizing the orthogonality of the modal mass normalized shapes.

$$\begin{bmatrix} 1 & & \\ & 1 & \\ & & \ddots \\ & & & 1 \end{bmatrix} \begin{bmatrix} \ddot{q}_{ij,1} \\ \ddot{q}_{ij,2} \\ \vdots \\ \ddot{q}_{ij,n} \end{bmatrix} + \begin{bmatrix} 2\xi_{ij,1}\omega_{ij,1} & & & \\ & 2\xi_{ij,2}\omega_{ij,2} & & \\ & & \ddots & \\ & & & 2\xi_{ij,n}\omega_{ij,n} \end{bmatrix} \begin{bmatrix} q_{ij,1} \\ q_{ij,2} \\ \vdots \\ q_{ij,n} \end{bmatrix} + \begin{bmatrix} \omega_{ij,1}^2 & & & \\ & \omega_{ij,2}^2 & & \\ & & \ddots & \\ & & & \omega_{ij,n}^2 \end{bmatrix} \begin{bmatrix} q_{ij,1} \\ q_{ij,2} \\ \vdots \\ q_{ij,n} \end{bmatrix}$$
$$= \begin{bmatrix} u_{ij,11} \\ u_{ij,12} \\ \vdots \\ u_{ij,1n} \end{bmatrix} f_{ij,1}(t) \quad (i,j=x,y) \tag{22}$$

To add the forces $f_{xx,1}(t)$ and $f_{xy,1}(t)$,$f_{yx,1}(t)$, and $f_{yy,1}(t)$ in Eq. (22), the matrixes U_{ij} satisfying the following conditions are constructed.

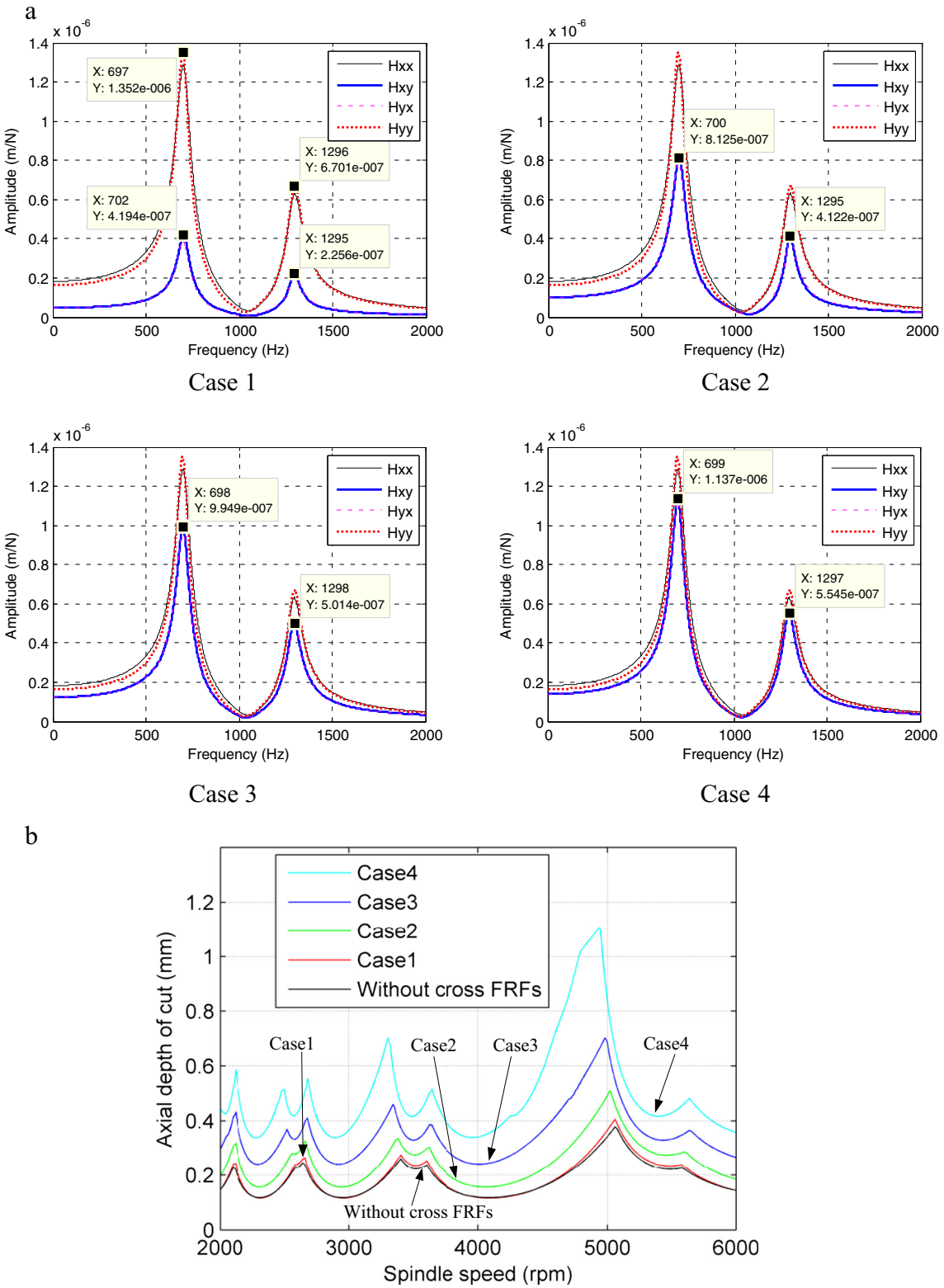

Fig. 9 Stability lobe variation with the cross-FRFs: **a** the magnitude of the cross-FRFs H_{xy} and H_{yx} with four cases compared with the direct FRFs H_{xx} and H_{yy} and **b** stability lobe variation with the four cases

Table 3 Tool parameters of the cutter

Diameter (mm)	Number of flutes	Helix angle (°)	Flute length (mm)	Cutter overhang (mm)	Cutter material
16	4	50	42	97	Carbide alloy

$$U_{ij}\begin{bmatrix} u_{ij,11} \\ u_{ij,12} \\ \vdots \\ u_{ij,1n} \end{bmatrix} = \begin{bmatrix} 1 \\ 1 \\ \vdots \\ 1 \end{bmatrix} \Rightarrow U_{ij} = \begin{bmatrix} 1/u_{ij,11} & & & \\ & 1/u_{ij,12} & & \\ & & \ddots & \\ & & & 1/u_{ij,1n} \end{bmatrix} \quad (i = x, y \quad j = x, y) \tag{23}$$

Equation (22) is multiplied by the U_{ij} and can be expressed as

$$U_{ij}\begin{bmatrix} 1 & & & \\ & 1 & & \\ & & \ddots & \\ & & & 1 \end{bmatrix}\begin{bmatrix} \ddot{q}_{ij,1} \\ \ddot{q}_{ij,2} \\ \vdots \\ \ddot{q}_{ij,n} \end{bmatrix} + U_{ij}\begin{bmatrix} 2\xi_{ij,1}\omega_{ij,1} & & & \\ & 2\xi_{ij,2}\omega_{ij,2} & & \\ & & \ddots & \\ & & & 2\xi_{ij,n}\omega_{ij,n} \end{bmatrix}\begin{bmatrix} q_{ij,1} \\ q_{ij,2} \\ \vdots \\ q_{ij,n} \end{bmatrix} + U_{ij}\begin{bmatrix} \omega_{ij,1}^2 & & & \\ & \omega_{ij,2}^2 & & \\ & & \ddots & \\ & & & \omega_{ij,n}^2 \end{bmatrix}\begin{bmatrix} q_{ij,1} \\ q_{ij,2} \\ \vdots \\ q_{ij,n} \end{bmatrix}$$
$$= \begin{bmatrix} 1 \\ 1 \\ \vdots \\ 1 \end{bmatrix} f_{ij,1}(t) \quad (i, j = x, y) \tag{24}$$

Substituting Eq. (21) into Eq. (24) and adding the force $f_{ij,1}(t)(i,j=x,y)$ according to $f_{xx,1}(t)+f_{xy,1}(t)=f_x(t)$ and $f_{yx,1}(t)+f_{yy,1}(t)=f_y(t)$, the dynamic equation in modal space can be obtained as follows:

$$\begin{bmatrix} \tilde{\mathbf{M}}_{xx} & \tilde{\mathbf{M}}_{xy} \\ \tilde{\mathbf{M}}_{yx} & \tilde{\mathbf{M}}_{yy} \end{bmatrix}\begin{bmatrix} \ddot{\mathbf{q}}_x(t) \\ \ddot{\mathbf{q}}_y(t) \end{bmatrix} + \begin{bmatrix} \tilde{\mathbf{C}}_{xx} & \tilde{\mathbf{C}}_{xy} \\ \tilde{\mathbf{C}}_{yx} & \tilde{\mathbf{C}}_{yy} \end{bmatrix}\begin{bmatrix} \mathbf{q}_x(t) \\ \mathbf{q}_y(t) \end{bmatrix} + \begin{bmatrix} \tilde{\mathbf{K}}_{xx} & \tilde{\mathbf{K}}_{xy} \\ \tilde{\mathbf{K}}_{yx} & \tilde{\mathbf{K}}_{yy} \end{bmatrix}\begin{bmatrix} \mathbf{q}_x(t) \\ \mathbf{q}_y(t) \end{bmatrix}$$
$$= \mathbf{B}(t)\left[\begin{bmatrix} \mathbf{q}_x(t) \\ \mathbf{q}_y(t) \end{bmatrix} - \begin{bmatrix} \mathbf{q}_x(t-T) \\ \mathbf{q}_y(t-T) \end{bmatrix}\right] \tag{25}$$

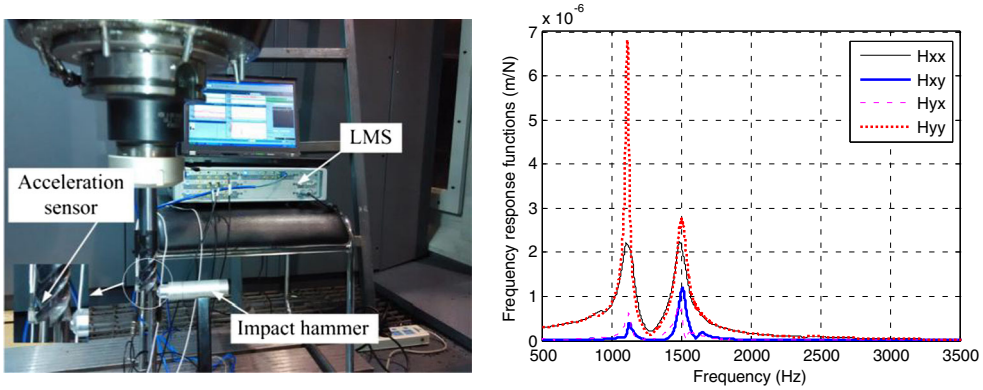

Fig. 10 Impact experiment and FRFs of the tool tip

Table 4 Fitted modal parameters

		Frequency (Hz)	Damping (%)	Residue
xx	First mode	1109	3.05	1.195e−004−4.517e−004j
	Second mode	1494	2.65	−1.238e−004−5.031e−004j
xy	First mode	1135	1.79	1.101e−005−3.040e−005j
	Second mode	1510	1.18	3.901e−005−7.436e−005j
yx	First mode	1130	1.28	−2.515e−006−4.941e−005j
	Second mode	1487	1.20	−4.166e−005−7.996e−005j
yy	First mode	1116	0.90	−1.669e−005−4.487e−004j
	Second mode	1498	2.18	−6.263e−005−5.480e−004j

where

$$\mathbf{q}_x(t) = \begin{bmatrix} q_{xx,1} & q_{xx,2} & \cdots & q_{xx,n} \end{bmatrix}^{\mathrm{T}}$$
$$\mathbf{q}_y(t) = \begin{bmatrix} q_{yy,1} & q_{yy,2} & \cdots & q_{yy,n} \end{bmatrix}^{\mathrm{T}}$$

$$\tilde{\mathbf{M}}_{xx} = \mathrm{diag}\left(1/u_{xx,11} \quad 1/u_{xx,12} \quad \cdots \quad 1/u_{xx,1n} \right)$$
$$\tilde{\mathbf{M}}_{xy} = \mathrm{diag}\left(u_{yy,11}/u_{xy,11}^2 \quad u_{yy,12}/u_{xy,12}^2 \quad \cdots \quad u_{yy,1n}/u_{xy,1n}^2 \right)$$
$$\tilde{\mathbf{M}}_{yx} = \mathrm{diag}\left(u_{xx,11}/u_{yx,11}^2 \quad u_{xx,12}/u_{yx,12}^2 \quad \cdots \quad u_{xx,1n}/u_{yx,1n}^2 \right)$$
$$\tilde{\mathbf{M}}_{yy} = \mathrm{diag}\left(1/u_{yy,11} \quad 1/u_{yy,12} \quad \cdots \quad 1/u_{yy,1n} \right)$$

$$\tilde{\mathbf{C}}_{xx} = \mathrm{diag}\left(2\xi_{xx,1}\omega_{xx,1}/u_{xx,11} \quad 2\xi_{xx,2}\omega_{xx,2}/u_{xx,12} \quad \cdots \quad 2\xi_{xx,n}\omega_{xx,n}/u_{xx,1n} \right)$$
$$\tilde{\mathbf{C}}_{xy} = \mathrm{diag}\left(2\xi_{xy,1}\omega_{xy,1}u_{yy,11}/u_{xy,11}^2 \quad 2\xi_{xy,2}\omega_{xy,2}u_{yy,12}/u_{xy,12}^2 \quad \cdots \quad 2\xi_{xy,n}\omega_{xy,n}u_{yy,1n}/u_{xy,1n}^2 \right)$$
$$\tilde{\mathbf{C}}_{yx} = \mathrm{diag}\left(2\xi_{yx,1}\omega_{yx,1}u_{xx,11}/u_{yx,11}^2 \quad 2\xi_{yx,2}\omega_{yx,2}u_{xx,12}/u_{yx,12}^2 \quad \cdots \quad 2\xi_{yx,n}\omega_{yx,n}u_{xx,1n}/u_{yx,1n}^2 \right)$$
$$\tilde{\mathbf{C}}_{yy} = \mathrm{diag}\left(2\xi_{yy,1}\omega_{yy,1}/u_{yy,11} \quad 2\xi_{yy,2}\omega_{yy,2}/u_{yy,12} \quad \cdots \quad 2\xi_{yy,n}\omega_{yy,n}/u_{yy,1n} \right)$$

$$\tilde{\mathbf{K}}_{xx} = \mathrm{diag}\left(\omega_{xx,1}^2/u_{xx,11} \quad \omega_{xx,2}^2/u_{xx,12} \quad \cdots \quad \omega_{xx,n}^2/u_{xx,1n} \right)$$
$$\tilde{\mathbf{K}}_{xy} = \mathrm{diag}\left(\omega_{xy,1}^2u_{yy,11}/u_{xy,11}^2 \quad \omega_{xy,2}^2u_{yy,12}/u_{xy,12}^2 \quad \cdots \quad \omega_{xy,n}^2u_{yy,1n}/u_{xy,1n}^2 \right)$$
$$\tilde{\mathbf{K}}_{yx} = \mathrm{diag}\left(\omega_{yx,1}^2u_{xx,11}/u_{yx,11}^2 \quad \omega_{yx,2}^2u_{xx,12}/u_{yx,12}^2 \quad \cdots \quad \omega_{yx,n}^2u_{xx,1n}/u_{yx,1n}^2 \right)$$
$$\tilde{\mathbf{K}}_{yy} = \mathrm{diag}\left(\omega_{yy,1}^2/u_{yy,11} \quad \omega_{yy,2}^2/u_{yy,12} \quad \cdots \quad \omega_{yy,n}^2/u_{yy,1n} \right)$$

$$\mathbf{B}(t) = \begin{bmatrix} a_{xx} & a_{xy} & 0 & 0 & 0 & 0 & \cdots & 0 \\ a_{xx} & a_{xy} & 0 & 0 & 0 & 0 & \cdots & 0 \\ \vdots & \vdots & \vdots & \vdots & \vdots & \vdots & \cdots & \vdots \\ a_{xx} & a_{xy} & 0 & 0 & 0 & 0 & \cdots & 0 \\ 0 & 0 & 0 & 0 & \cdots & 0 & a_{yx} & a_{yy} \\ 0 & 0 & 0 & 0 & \cdots & 0 & a_{yx} & a_{yy} \\ \vdots & \vdots & \vdots & \vdots & \cdots & \vdots & \vdots & \vdots \\ 0 & 0 & 0 & 0 & \cdots & 0 & a_{yx} & a_{yy} \end{bmatrix} \begin{bmatrix} u_{xx,11} & u_{xx,12} & \cdots & u_{xx,1n} & 0 & 0 & \cdots & 0 \\ 0 & 0 & \cdots & 0 & u_{yy,11} & u_{yy,12} & \cdots & u_{yy,1n} \\ 0 & 0 & 0 & 0 & 0 & 0 & \cdots & 0 \\ 0 & 0 & 0 & 0 & 0 & 0 & \cdots & 0 \\ \vdots & \vdots & \vdots & \vdots & \vdots & \vdots & \cdots & 0 \\ 0 & 0 & 0 & 0 & 0 & 0 & \cdots & \vdots \\ u_{xx,11} & u_{xx,12} & \cdots & u_{xx,1n} & 0 & 0 & \cdots & 0 \\ 0 & 0 & \cdots & 0 & u_{yy,11} & u_{yy,12} & \cdots & u_{yy,1n} \end{bmatrix}$$

The modal parameters ξ and ω in Eq. (25) and residues are identified by the FRFs H' in Eq. (5). According to [25], the modal shapes $u_{ij,1l}(\, i,j = x,y \quad l = 1,2,\cdots,n\,)$ in Eq. (25) can be got by the relationship of the modal shapes and residues.

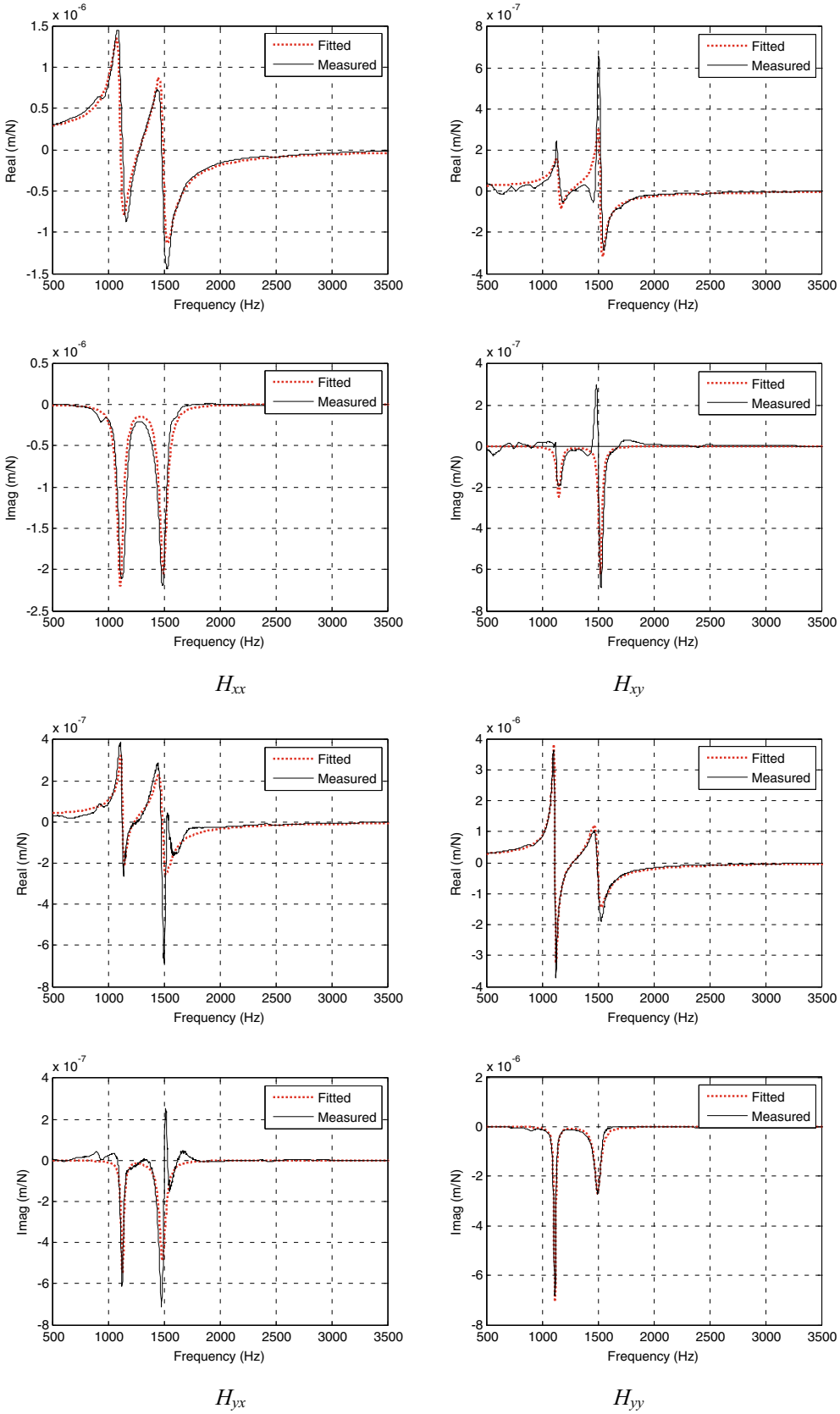

Fig. 11 Fitted and measured frequency response functions

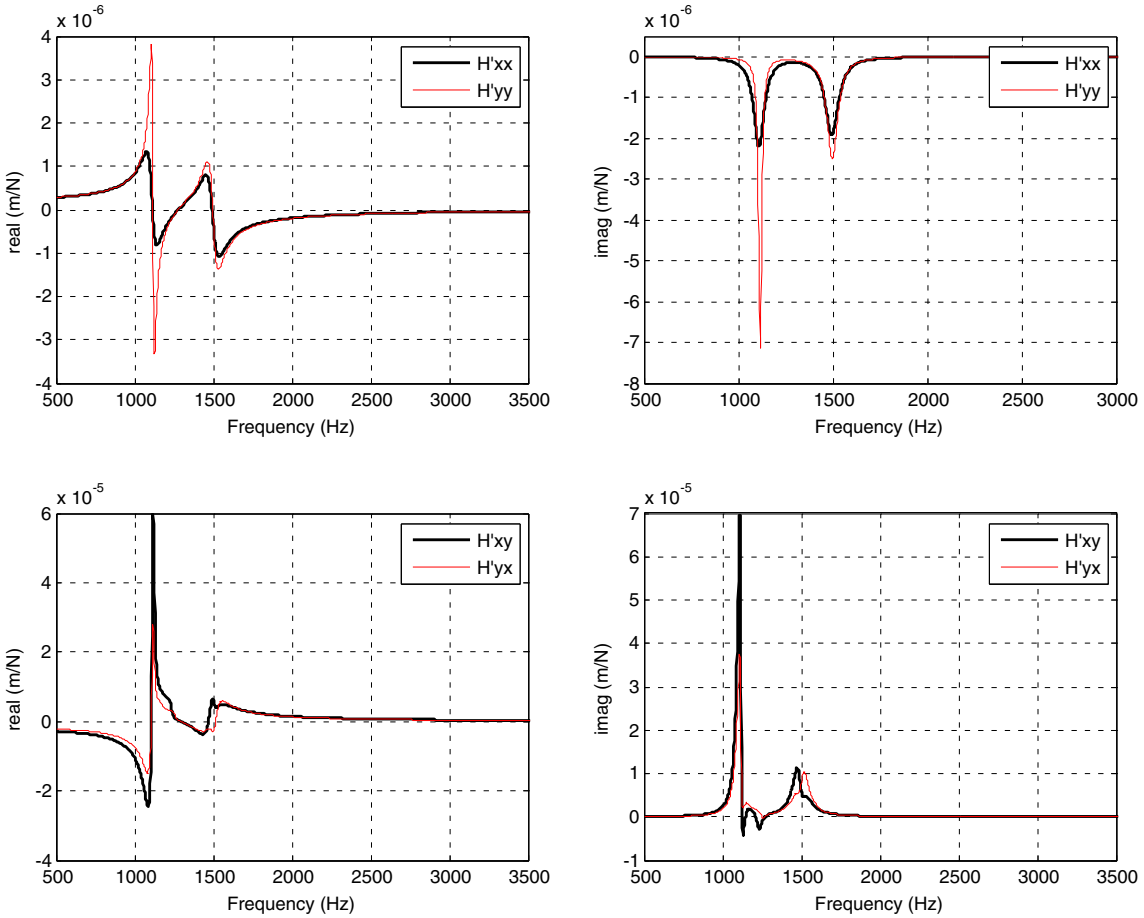

Fig. 12 The transformed FRFs

Note that since the residues are complex numbers, the resulting mode shapes will be complex and depend on the damped natural frequency ω_d. It is possible to obtain simplified real mode shapes from the residues by considering that the structures have proportional damping and discarding the imaginary parts of the complex mode shapes [25].

3 Numerical simulation and analysis

The frequency domain method ZOA [12] can achieve an accurate milling stability prediction simultaneously considering multiple modes and the cross-FRFs by scanning the chatter frequencies around all of the dominant modes of the transfer

Table 5 Modal parameters identified by the FRFs in Fig. 12

		Frequency (Hz)	Damping (%)	Residue
xx	First mode	1109	3.05	−1.270e−006−4.613e−004j
	Second mode	1494	2.67	−8.610e−007−4.914e−004j
xy	First mode	1116	0.90	4.109e−003+3.306e−003j
	Second mode	1492	2.57	1.437e−003+3.485e−003j
yx	First mode	1116	0.91	1.443e−003+2.102e−003j
	Second mode	1523	2.18	3.024e−004+1.748e−003j
yy	First mode	1116	0.90	−3.465e−006−4.488e−004j
	Second mode	1497	2.21	−2.325e−006−5.322e−004j

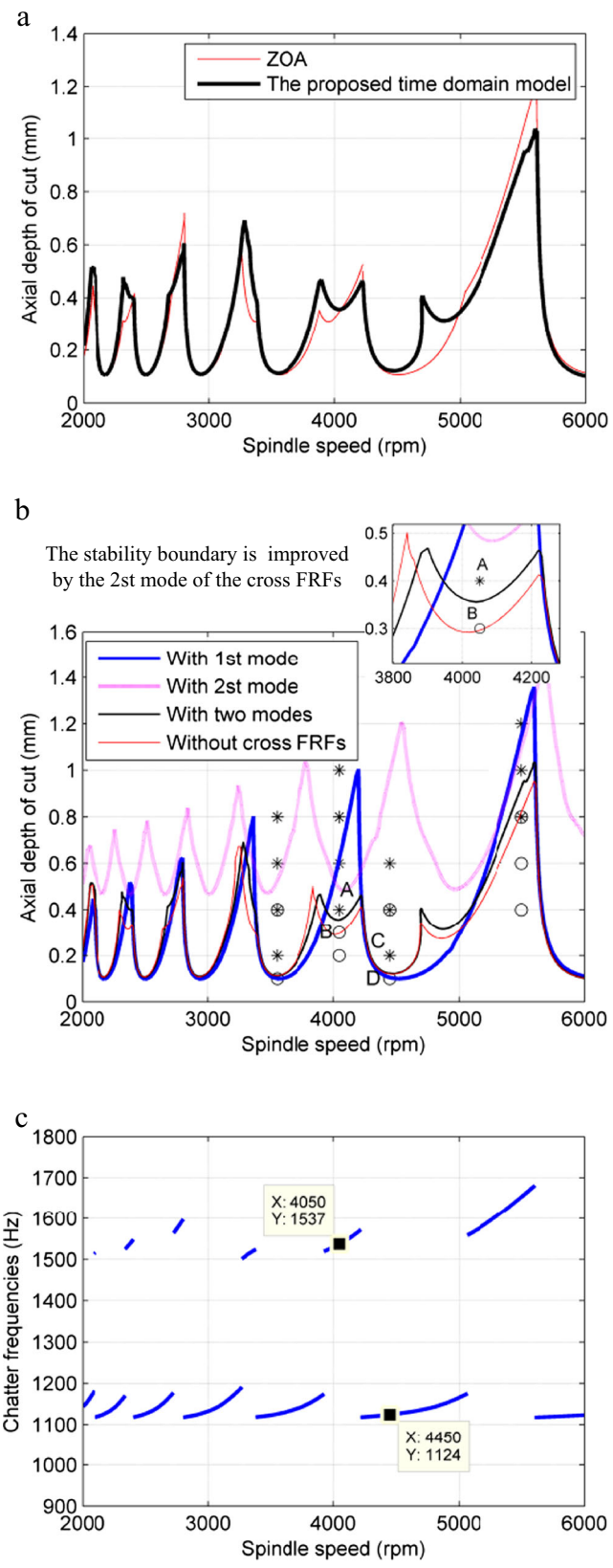

Fig. 13 Theoretical stability boundaries with the corresponding chatter frequencies and experimental results. The *symbols* are follows: (1) *open circle* is clearly stable case, (2) *asterisk* is clearly unstable cutting test, and (3) ⊗ is not clearly stable or unstable

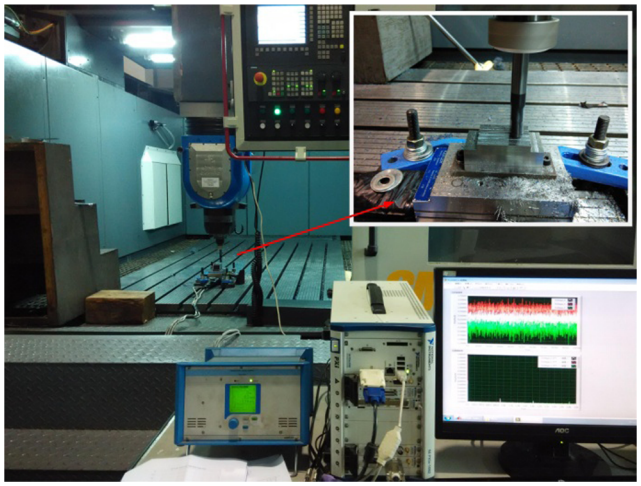

Fig. 14 Cutting experiment

functions and introducing the cross-FRFs in the eigenvalue equation. To verify the effectiveness of the proposed time domain model for the accurate milling stability prediction, the stability lobes obtained by the proposed model are compared with those from the ZOA method. The proposed time domain model is solved by utilizing the FDM [18].

The modal parameters with two modes in Table 1 are illustrated for the stability lobe calculation of the proposed time domain model and frequency domain method ZOA.According to the modal parameters in Table 1, the FRFs based on the modal shape fitting are shown in Fig. 4.By referring to Eq. (5), the transformed FRFs calculated by the FRFs in Fig. 4 are shown in Fig. 5.

The modal parameters are identified by using the PloyMAX modules of LMS Test. Lab® from the FRFs in Fig. 5 and are shown in Table 2.

A four-fluted cutter with no helix angle and the cutting force coefficients K_t=3127Mpa and K_r=1769Mpa are used in the calculation. The simulations are performed using the proposed time domain model and ZOA method for up-milling. The large radial depths of cut ratios a/D= 0.5 and a/D= 1 are adopted in simulations for reducing the influence of the neglected harmonic components in the ZOA method. The proposed time domain model is solved by the FDM with a discrete number m=40 over a 200×100 sized grid. From the stability lobes in Fig. 6, it is noted that the stability boundary of the proposed time domain model is in agreement with the ZOA method, which verifies the effectiveness of the proposed time domain model for the milling stability prediction considering multiple modes and the cross-FRFs simultaneously.

The effects of multiple modes and cross-FRFs on the stability boundary are analyzed. As seen in Fig. 7, it is noted that the two modes influence each other on the stability boundary, especially on the third and fourth peaks of the lobes. Consequently, point A is stable in the stability lobes when only considering the second mode, but it is unstable when

Fig. 15 Force signal and force spectrum of F_x at different parameter points

Point A (chatter)

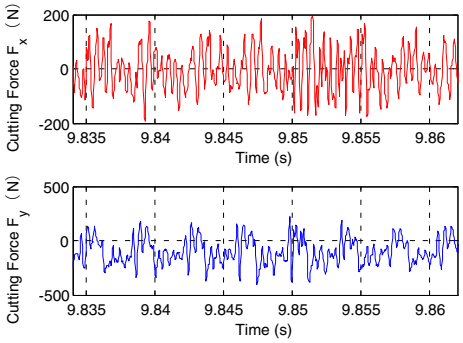

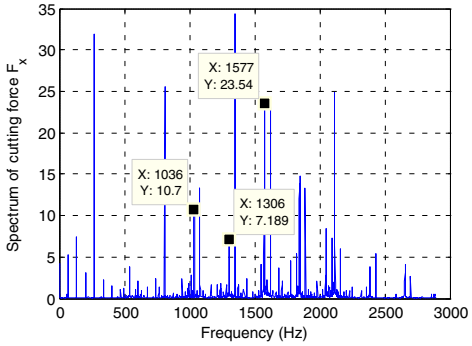

Point B (stable)

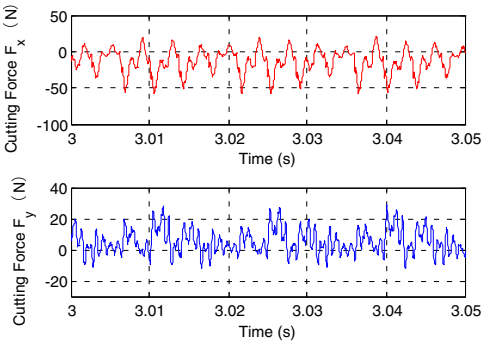

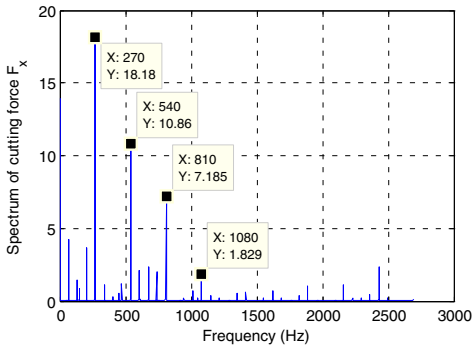

Point C (chatter)

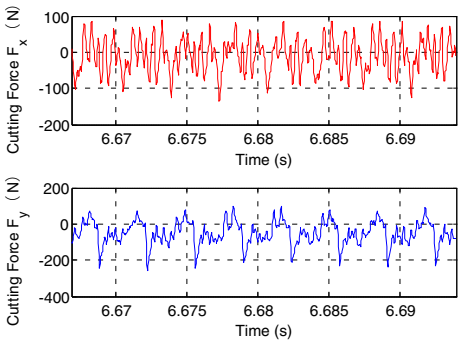

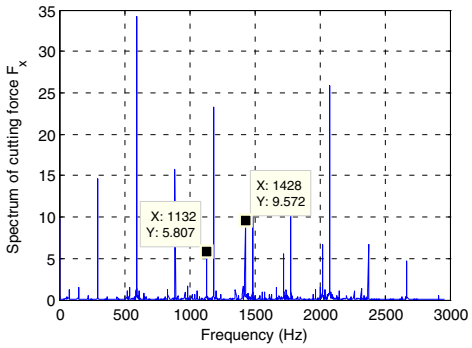

Point D (stable)

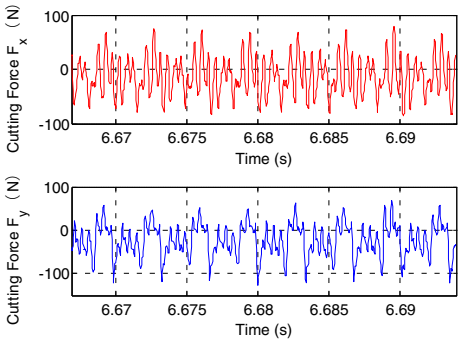

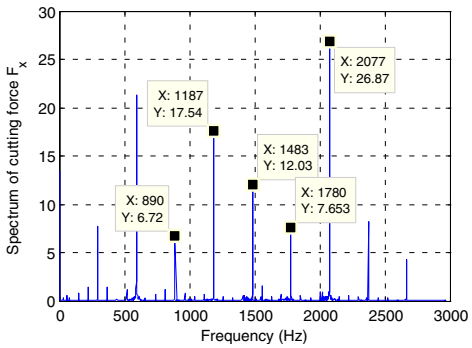

considering both modes. Point B is stable in the stability lobes when only considering the first mode, but it is unstable when considering both modes. Points C and D are the actual machining parameters without the occurrence of chatter.

In addition to the effect of multiple modes, the stability boundary is also influenced by the cross-FRFs. In Fig. 8, it can be found that the cross-FRFs increase the stability boundary compared with the case where the cross-FRFs are neglected.

Since the cross-FRFs have influence on the stability boundary, it is reasonable to analyze the influence of the magnitude variation of the cross-FRF H_{xy} and H_{yx} on stability boundary. Four cases of different magnitude of the cross-FRF H_{xy} and H_{yx} compared with the fixed direct FRF H_{xx} and H_{yy} are performed to show this influence, as shown in Fig. 9.

As seen in Fig. 9, when the amplitude of the first mode of cross-FRFs increases from 0 m/N (without cross-FRFs) to 4.194×10^{-7} m/N (case 1), the stability boundary barely changes. However, in the similar amplitude difference 4×10^{-7} m/N, the stability boundary increases significantly while the amplitude increases from 4.194×10^{-7} m/N (case 1) to 8.125×10^{-7} m/N (case 2). Furthermore, the stability boundary increases greatly when the amplitude increases from 9.949×10^{-7} m/N (case 3) to 1.137×10^{-7} m/N (case 4) and has only 1.88×10^{-7} m/N difference. This indicates that the magnitude of the cross-FRFs compared with the direct FRFs is an essential factor influencing the stability boundary. When the amplitude ratio of the cross-FRFs and direct FRFs is greater than 0.5, such as case 2, the cross-FRFs should be considered in the stability prediction.

4 Experimental validation

From the above numerical simulation analysis, the effectiveness of the proposed time domain model for milling stability prediction considering multiple modes and cross-FRFs simultaneously is verified. Meanwhile, it is known that the interactions between multiple modes and the cross-FRFs both have effect on the stability boundary. In this section, one experimental case is studied to verify the effectiveness of the proposed time domain model. In the experimental case, the FRFs including the cross-FRFs should be acquired and analyzed by the modal testing experiment. The cutting force coefficients for the particular cutter and workpiece material are calibrated by cutting force experiments.

4.1 Calibration of cutting force coefficients

A four-fluted helical mill cutter is used in the experiment, and the parameters of the tool are listed in Table 3. The material used in the experiment is the high-strength steel 300 M, which easily produces the chatter phenomenon due to its high hardness after heat treatment. Using the milling force model [26], the cutting force coefficients, K_t=3127 MPa and K_r= 1769 MPa, are calibrated by the experiment.

4.2 Identification of modal parameters

The modal parameters are obtained by a modal impact experiment on a five-axis gantry machining center GMC 1600H/2. The exciting force on the tool tip is applied by a PCB impact hammer 086C03, and the vibration signal of tool tip is acquired by a DYTRAN acceleration sensor 3224A1. LMS is used for data acquisition and modal analysis. The modal impact experiment is shown in Fig. 10a. The modal impact testing is conducted five times in each direction, and the FRF is averaged to reduce the impact uncertainty. The FRFs of the tool tip are shown in Fig. 10b. It is clear that the direct FRFs and cross-FRFs all have two modes (approximately 1115 and 1500 Hz).

The modal parameters are fitted using the PloyMAX modules of LMS Test. Lab® in the frequency range 500–3500 Hz. The fitted modal parameters are listed in Table 4. The measured FRF and fitted curves are plotted in Fig. 11.

According to the explanation in Sect. 2, the transformed FRFs H' should be calculated as Eq. (5) for the stability calculation when the cross-FRFs is considered. The transformed FRFs are shown in Fig. 12, and the corresponding modal parameters identified using the PloyMAX modules of LMS Test. Lab® are listed in Table 5.

4.3 Comparison between stability prediction and experiment

The milling stability prediction is performed using the modal parameters identified in Table 5 with a radial depth of cut ratios a/D=0.25 and a feed per tooth f_z=0.07. Figure 13a shows the stability lobes with the proposed time domain model and the ZOA method. The stability lobes with multiple modes and the cross-FRFs are shown in Fig. 13b. The stability predictions with single mode or no cross-FRF effect are also plotted in Fig. 13b for comparison and analysis. Theoretical chatter frequencies on the stability boundary are shown in Fig. 13c.

A cutting experiment is performed to verify the stability prediction of the proposed time domain model, as shown in Fig. 14. During the experiment, a KISTLER 9257A dynamometer and an NI PXIe-4499 data acquisition module are used to record the force signals. The sampling rate is set to 30 kHz. The experiment results are plotted in Fig. 13b for comparison with the theoretical prediction. The experimental results agree well with the prediction.

The measured FRFs of the tool tip in Fig. 10 show that the first mode amplitude of the cross-FRFs is much smaller than that of the direct FRFs, while the second mode amplitude of

the cross-FRFs is nearly half of that of the direct FRFs. According to the influences of multiple modes and cross-FRFs on stability boundary, which are analyzed above, the second mode of the cross-FRFs will improve the stability boundary on the peaks of the lobe. The result of the stability boundary improvement is shown in Fig. 13b.

The cutting forces at some parameter points (A, B, C, D) are illustrated, and the spectrum of F_x is analyzed. Figure 15 shows the cutting force and the spectrum of F_x. The force spectrum in the x direction of point A (4050 rpm, 0.4 mm) has the chatter frequencies of 1036, 1306, and 1577 Hz. The differences are 270 and 271 Hz, which are equal to the tooth passing frequency (4050/60×4=270 Hz). The chatter frequency (1577 Hz) is close to the theoretical chatter frequency (1537 Hz) of the stability boundary shown in Fig. 13c. On the other hand, in point B (4050 rpm, 0.2 mm), only the harmonic vibration frequencies (270, 540, 810, 1080 Hz, etc.) appear, where frequencies are integral multiples of the spindle speed frequency (4050/60=67.5 Hz). Point C (4450 rpm, 0.2 mm) is unstable due to the occurrence of chatter frequencies (1132 and 1428 Hz). The chatter frequency (1132 Hz) is close to the theoretical chatter frequency (1124 Hz) of the stability boundary shown in Fig. 13c. Point D (4450 rpm, 0.1 mm) is stable, and the corresponding frequencies (890, 1187, 1483, 1780, 2077 Hz, etc.) in the spectrum are all of the harmonic vibration frequencies. Above all, the comparisons show that the milling stability prediction is in good agreement with the experimental results. Consequently, in addition to the theoretical simulation verification in Sect. 3, the proposed time domain model simultaneously considering multiple modes and cross-FRFs has proved effective from the experiments.

From the theoretical prediction and experimental results as seen in Fig. 13b, the multi-mode interaction and cross-FRFs both affect the accurate prediction of the stability lobe diagram.

As seen in Fig. 13b, the two modes have great influence on the stability boundary, especially on the second, fifth, and sixth peaks of the lobe. The second mode reduces the stability boundary on the basis of the first mode in the overlapping region. And, as shown in Fig. 13c, the theoretical chatter frequencies on the peaks of the lobe diagram are close to the second mode frequency of the tool tip. The chatter frequencies on the troughs of the lobe diagram are close to the first mode frequency of the tool tip. According to the chatter theory researched by Altintas [13, 25], chatter appears around the mode frequency. Thus, one stability point according to one mode may be the chatter point when the chatter frequency of this point locates around another mode.

In addition to the effect of multiple modes, it can be seen in Fig. 13b that the cross-FRFs increase the stability boundary compared with the case where the cross-FRFs are neglected. The reason may be as follows [11].

Chatter is a kind of mechanism, which transfers energy into the structure to sustain the vibration. The major part of the energy is used for direct vibration (the exCitation in one direction causes vibrations in the same direction) if the cross-FRFs are neglected. When the cross-FRFs are simultaneously considered, the transferred energy is scattered (the exCitation in one direction causes vibrations in two directions). If we want to make the structure chatter still happen, more energy is needed, which is reflected in the large cutting depth. So, the stability boundary is increasing.

5 Conclusions

In this paper, an effective time domain model simultaneously considering multiple modes and cross-FRFs was proposed. In the dynamic equation, the number of vibration variables is more than the number of matrix dimensions due to the introduction of the multiple modes. The approaches of multiple modal parameter normalization on the tool tip and reducing the vibration variable number in modal space are described in detail and proven effective. When considering the cross-FRF effect, the mechanical mobility and impedance transformation method was proposed to calculate the transformed FRFs for modeling of stability prediction. The comparisons of the numerical simulation results between the proposed time domain model and the frequency domain method ZOA demonstrate the effectiveness of the proposed model. In addition, a cutting experiment was performed, and the results are in good agreement with the stability prediction. The proposed time domain model was verified by the numerical simulation results and the cutting experiment.

On the basis of the accurate prediction of stability lobe diagram, the effect of multiple modes and cross-FRFs on the stability boundary was analyzed. By comparing the stability boundary with different magnitude of the cross-FRFs H_{xy} and H_{yx}, it indicates that the amplitude ratio of the cross-FRFs and direct FRFs is an essential factor influencing the stability boundary. The stability boundary improves with the increasing amplitude ratio. When the amplitude ratio of the cross-FRFs and direct FRFs is greater than 0.5, the cross-FRFs have significant effect on the stability prediction.

Acknowledgments This work was partially supported by the National Natural Science Foundation of China under Grant No. 51275189, the Project of Key Technology Innovation Project of Hubei Province under Grant No. 2013AAA008, and the National Natural Science Foundation of China under Grant No. 51421062.

References

1. Tlusty J, Polacek M (1963) The stability of machine tools against self excited vibrations in machining. Int Res Prod Eng 1:465–474
2. Smith S, Tlusty J (1991) An overview of modeling and simulation of the milling process. J Eng Ind 113:169–175
3. Yang YQ, Liu Q, Zhang B (2014) Three-dimensional chatter stability prediction of milling based on the linear and exponential cutting force model. Int J Adv Manuf Technol 72:1175–1185
4. Wang MH, Gao L, Zheng YH (2014) Prediction of regenerative chatter in the high-speed vertical milling of thin-walled workpiece made of titanium alloy. Int J Adv Manuf Technol 72:707–716
5. Solis E, Peres CR, Jiménez JE, Alique JR, Monje JC (2004) A new analytical-experimental method for the identification of stability lobes in high-speed milling. Int J Mach Tools Manuf 44:1591–1597
6. Mann BP, Young KA, Schmitz TL, Dilley DN (2005) Simultaneous stability and surface location error predictions in milling. J Manuf Sci Eng 127:446–453
7. Tang WX, Song QH, Yu SQ, Sun SS, Li BB, Du B, Ai X (2009) Prediction of chatter stability in high-speed finishing end milling considering multi-mode dynamics. J Mater Process Technol 209: 2585–2591
8. Wan M, Ma YC, Zhang WH, Yang Y (2015) Study on the construction mechanism of stability lobes in milling process with multiple modes. Int J Adv Manuf Technol 79:589–603
9. Berglind L, Ziegert J (2015) Analytical time-domain turning model with multiple modes. CIRP Ann Manuf Technol 64:137–140
10. Cao H, Li B, He Z (2012) Chatter stability of milling with speed-varying dynamics of spindles. Int J Mach Tools Manuf 52:50–58
11. Zhang XJ, Xiong CH, Ding Y, Feng MJ, Xiong YL (2012) Milling stability analysis with simultaneously considering the structural mode coupling effect and regenerative effect. Int J Mach Tools Manuf 53:127–140
12. Altintas Y, Budak E (1995) Analytical prediction of stability lobes in milling. CIRP Ann Manuf Technol 44:357–362
13. Merdol SD, Altintas Y (2004) Multi frequency solution of chatter stability for low immersion milling. J Manuf Sci Eng 126:459–466
14. Bachrathy D, Stepan G (2013) Improved prediction of stability lobes with extended multi frequency solution. CIRP Ann Manuf Technol 62:411–414
15. Bayly PV, Halley JE, Mann BP, Davies MA (2003) Stability of interrupted cutting by temporal finite element analysis. J Manuf Sci Eng 125:220–225
16. Insperger T, Stépán G (2002) Semi-discretization method for delayed systems. Int J Numer Methods Eng 55:503–518
17. Insperger T, Stépán G (2004) Updated semi-discretization method for periodic delay-differential equations with discrete delay. Int J Numer Methods Eng 64:117–141
18. Ding Y, Zhu LM, Zhang XJ, Ding H (2010) A full-discretization method for prediction of milling stability. Int J Mach Tools Manuf 50:502–509
19. Ding Y, Zhu LM, Zhang XJ, Ding H (2011) Numerical integration method for prediction of milling stability. J Manuf Sci Eng 133: 031005
20. Liang XG, Yao ZQ, Luo L, Hu J (2013) An improved numerical integration method for predicting milling stability with varying time delay. Int J Adv Manuf Technol 68:1967–1976
21. Niu JB, Ding Y, Zhu LM, Ding H (2014) Runge–Kutta methods for a semi-analytical prediction of milling stability. Nonlinear Dyn 76: 289–304
22. Gradišek J, Kalveram M, Insperger T, Weinert K, Stépán G, Govekar E, Grabec I (2005) On stability prediction for milling. Int J Mach Tools Manuf 45:769–781
23. Mann BP, Edes BT, Easley SJ, Young KA, Ma K (2008) Chatter vibration and surface location error prediction for helical end mills. Int J Mach Tools Manuf 48:350–361
24. Munoa Dombovari JZ, Mancisidor I, Yang YQ, Zatarain M (2013) Interaction between multiple modes in milling processes. Mach Sci Technol 17:165–180
25. Altintas Y (2000) Manufacturing automation: metal cutting mechanics, machine tool vibrations, and CNC design. Cambridge University Press, Cambridge
26. Budak E, Altintas Y, Armarego EJA (1996) Prediction of milling force coefficients from orthogonal cutting data. J Manuf Sci Eng 118:216–224